LANGMUIR

pubs.acs.org/Langmuir Article

Particle Separation from Liquid Marbles by the Viscous Folding of Liquid Films

Yijun Feng, Guohua Liu,* Jinliang Xu,* Kaiying Wang, Wenbin Mao, and Guansheng Yao

Cite This: *Langmuir* 2022, 38, 2055−2065 Read Online

ACCESS | Metrics & More | Article Recommendations | Supporting Information

ABSTRACT: Particle separation from fluid interfaces is one of the major challenges due to the large capillary energy associated with particle adsorption. Previous approaches rely on physicochemical modification or tuning the electrostatic action. Here, we show experimentally that particle separation can be achieved by fast dynamics of drop impact on soap films. When a droplet wrapped with particles (liquid marble) collides with a soap film, it undergoes bouncing and coalescence, stripping and viscous separation, or tunneling through the film. Despite the violence of splashing events, the process robustly yields the stripping in a tunable range. This viscous separation is supported by the transfer front of dynamic contact among the film, particle crust, and drop and can be well controlled in a deterministic manner by selectable impact parameters. By extensive experiments, together with thermodynamic analysis, we disclose that the separation thresholds depend on the energy competition between the kinetic energy, the increased surface energy, and the viscous dissipation. The mechanical cracking of the particle crust arises from the complex coupling between interfacial stress and viscous forces. This study is of potential benefit in soft matter research and also permits the study of a drop with colloid and surface chemistry.

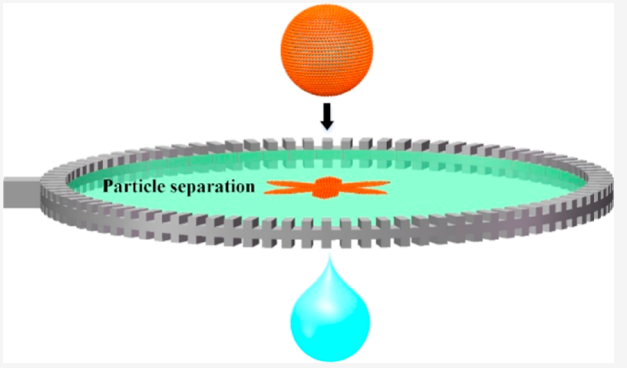

1. INTRODUCTION

Particle adsorption at fluid interfaces is a ubiquitous phenomenon that plays an important role in industries ranging from the health, environmental, food, to energy sectors.[1,2] For example, accumulation of dispersed particles at oil−water or air−water interfaces has been used to stabilize foams and Pickering emulsions in pharmaceutical,[3] food,[4,5] and cosmetic industries. Particle-encapsulated liquids have been adopted in miniature systems for biological and environmental applications, such as microarrays for high-throughput analyses and purifications.[6,7] The mining industry takes advantage of particle attachment to air bubbles to separate and recover valuable minerals.[8] The interfacial self-assembly of colloids provides unique opportunities to create novel materials with desired properties and functionality.[9−11] More recently, particle-stabilized emulsions are being explored to enhance oil recovery and biofuel conversion processes.[12,13]

Particles in the multiphase systems normally range in size from a few nanometers to tens of micrometers,[14] which have a strong tendency to adsorb at fluid interfaces. The driving force for this interfacial attachment is a reduction in interfacial energy. The adsorption is most favorable when the particle is wetted equally.[15] Even for nanoscale particles, this process is very robust and irreversible due to the large capillary energy associated with adsorption, typically many orders of magnitude larger than the thermal energy.[16] This strong attachment of particles at liquid interfaces is beneficial for engineering applications since they enhance stability,[17] but it poses significant challenges when particle separation is a requirement for sustainability and cost efficiency of the process.

Common approaches to particle separation rely on the physicochemical modification of the liquid phases. Desorption at the fluid interface has been achieved by adding a surface-active agent[18,19] or tuning the strength of electrostatic repulsion between particles through pH and electrolyte concentration.[20,21] Moreover, external fields have also been suggested for particle removal. A magnetic field has been used to destabilize emulsions of oil in water.[22] The gravitational field was responsible for the detachment of colloidal particles from drops of oil in water.[23,24] Alternatively, compressing the surface area results in mechanical desorption, as shown by ultrasound, cooling, or acoustic levitation desorption of colloids from particle-laden bubbles.[25−28] However, these methods for particle separation are either dependent on

Received: November 9, 2021
Revised: January 26, 2022
Published: February 4, 2022

https://doi.org/10.1021/acs.langmuir.1c02994
Langmuir 2022, 38, 2055−2065

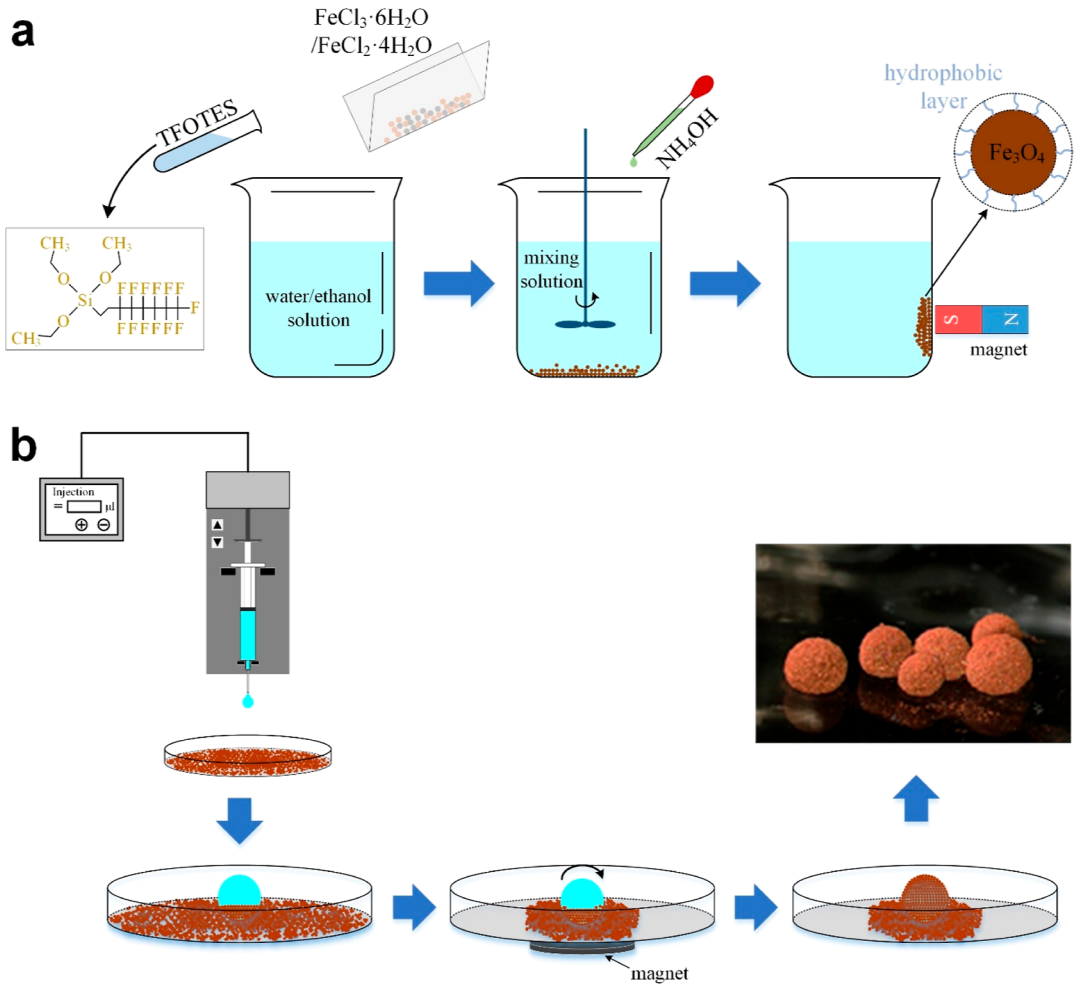

Figure 1. (a) Synthesis process of Fe_3O_4 nanoparticles. (b) Preparation process of the LMs.

specific particle properties or do not allow a precise control of release.

Here, we demonstrate a viscous separation concept by using a free-standing soap film as a physical separator to achieve particle separation from a fluid interface that cannot be attained by conventional technologies. High-speed imaging provides visual proof of dynamic modes when a liquid marble (LM) impacts a soap film. Within a tunable range of impact velocities, we observe that viscous separation of the nanoparticles from LMs occurs in a deterministic manner. The thermodynamic analysis further predicts the thresholds of such separation with a splash. This study highlights new phenomena associated with LMs' impact on liquid films, which could have far-reaching implications for the investigation of colloids and surface science.

2. MATERIALS AND METHODS

2.1. Materials. Ethanol, iron chloride hexahydrate ($FeCl_3·6H_2O$), iron(II) chloride tetrahydrate ($FeCl_2·4H_2O$), tridecafluorooctyltriethoxysilane (TFOTES) (97%), and sodium dodecyl sulfate (SDS) were purchased from Aladdin Biochemical Technology Co., Ltd. NH_4OH solution was purchased from Sigma-Aldrich. All the chemicals were used as received without further purification. Deionized water purchased from Beijing Fengyuhua Environmental Protection Technology Co., Ltd. was used for all experiments.

2.2. Preparation of Nanoparticles and LMs. First, 400 mL of water/ethanol solution with a volume ratio of 4:1 was prepared, and then $FeCl_3·6H_2O$ (1.70 g, 6.28 mmol), $FeCl_2·4H_2O$ (0.60 g, 3.02 mmol), and TFOTES (0.40 mL, 10.46 mmol) were dissolved in it. The aqueous NH_4OH solution (1.5 M) was added dropwise to the solution under nitrogen protection and vigorously stirred until it reached pH = 8. After stirring for 24 h, the resulting precipitate was isolated from the solution with a bar magnet, washed with a water/ethanol mixture three times, and dried at 60 °C (Figure 1a). The Fe_3O_4 powders were placed evenly on a glass dish. A droplet with a constant volume released by a precise microinjector was allowed to fall on the particle bed in the dish. A layer of particles adhered to the drop bottom. Then, a magnet was placed at the dish bottom to roll the droplet, wrapping the particles evenly on the drop surface (Figure 1b).

2.3. Preparation of the Liquid Film. To obtain the liquid film, the holding frame was prepared by a printing method. A photosensitive resin was selected as the printed material. A groove in the frame increased the liquid storage. The inner diameter, outer diameter, and thickness of the frame were 72, 80, and 4 mm, respectively. The depth of the groove was 1 mm, and the central angle corresponding to each groove was 2°. Both the upper and lower sides of the frame had grooves. Moreover, a soap solution consisting of stabilized materials could be obtained by mixing deionized water with SDS and guar powder. By varying the SDS concentration and adding guar powder, the lifetime and extensional rheology could be flexibly tuned. The soap film had good stability in this experiment with a surfactant concentration of 0.5 wt % and guar gum at 0.2 wt % (Table 1).

2.4. Experimental Methods. The transmission electron microscopy (TEM) images and elemental maps were obtained using a JEM 2100F operating in the bright-field mode with an accelerating voltage of 200 kV. X-ray diffraction (XRD) analysis was performed on a

https://doi.org/10.1021/acs.langmuir.1c02994
Langmuir 2022, 38, 2055−2065

Table 1. Physical Properties of the Soap Solution

physical parameters	value
density (kg/m^3)	830
viscosity (mPa·s)	6.48
surface tension (mN/m)	33.8

Bruker D8 ADVANCE X-ray diffractometer. X-ray photoelectron spectroscopy (XPS) measurements were performed on a Thermo Escalab 250xi instrument. A Shimadzu UV-3600 spectrometer was used to measure the UV−vis transmittance spectra.

For the impact experiment, the impact velocity was tuned by the falling height. The impact dynamics were traced from both the top and side view by using high-speed cameras (ImageIR 5380, InfraTec) at a frame rate of 3000 fps. We repeated a set of experiments for different impact velocities and LMs of different diameters (Table 2). Based on the sequential images, we calculated the impact velocity and recorded the dynamic trajectory.

Table 2. Dynamic Modes of LMs with Different Diameters and Heights

	diameter of LMs (mm)			
	impact state			
initial falling height (cm)	2.3	2.9	3.3	3.7
1.0	bouncing	bouncing	bouncing	bouncing
1.1	bouncing	bouncing	bouncing	bouncing
1.2	bouncing	bouncing	bouncing	stripping
1.3	bouncing	bouncing	bouncing	stripping
1.4	bouncing	bouncing	stripping	stripping
1.5	bouncing	bouncing	stripping	stripping
1.7	bouncing	bouncing	stripping	stripping
2.0	bouncing	stripping	stripping	tunneling
2.1	bouncing	stripping	stripping	tunneling
2.2	bouncing	stripping	tunneling	tunneling
2.3	bouncing	stripping	tunneling	tunneling
3.0	bouncing	stripping	tunneling	tunneling
3.1	stripping	tunneling	tunneling	tunneling
3.2	stripping	tunneling	tunneling	tunneling
3.3	stripping	tunneling	tunneling	tunneling
3.5	stripping	tunneling	tunneling	tunneling
4.0	stripping	tunneling	tunneling	tunneling
5.0	tunneling	tunneling	tunneling	tunneling

3. RESULTS AND DISCUSSION

3.1. Characterization. LMs are prepared by using hydrophobic Fe_3O_4 particles (Figure 2a).[29] The contact angle of a drop sitting on the particle bed is 120.9 ± 1.4° (Figure 2b). The TEM image shows that the particles have certain anisotropy, which can be approximately regarded as spherical with an average particle size of 13.4 nm (Figure 2c). Elemental mapping confirms the coexistence of Fe and O such that they are homogeneously dispersed on the powder surface (Figure 2d). The XRD pattern confirms the sharp peaks at 2θ = 30−80° that were assigned to (110), (220), (311), (400), (422), (511), (440), (620), and (533), which agree well with the crystallographic planes of Fe_3O_4 (Figure 2e).[30] The XPS pattern of the wide-scan spectrum of the particles (Figure 2f) is dominated by the signals of Fe, O, and C elements. The Fe $2p_{3/2}$ and Fe $2p_{1/2}$ core levels are present at 711.3 and 724.2 eV, respectively (Figure 2g), which are in association with the Fe_3O_4 crystallite in the carbon network.[31] The Fe 3p peak can be deconvoluted into the Fe^{2+} and Fe^{3+}peaks, and the total relative areas of the constituent peak are calculated. Since stoichiometric Fe_3O_4 can also be expressed to $FeO{\cdot}Fe_2O_3$, the Fe^{2+}/Fe^{3+}ratio should be 1:2 or 0.33:0.67. The deconvoluted peaks using the parameters defined above give Fe^{2+}/Fe^{3+} = 0.34:0.66, clearly indicating the stoichiometric oxide within the uncertainty of the calculations.

3.2. Design Principles and Impact Modes. Figure 3 shows a dynamic falling-impact process between a LM and a static soap film. The films consist of a stabilized reagent and other additives. Liquid molecules are held between two layers of surfactant molecules, creating a thin liquid film (inset of Figure 3).[32] By varying the surfactant concentration, we can tune the surface tension of the film in a certain range ∼ mN/m. To sustain the surface tension, a printed annular frame is used to hold the liquid film. When a LM with a diameter of d is released from an initial height h_0 onto the liquid film with a specific surface tension σ = 33.8 mN/m, one can notice that at certain values of initial height, the liquid drop passes through the film and the coated particles peel off from the LM. On the basis of experimental observation, we categorize the particle−film interactions into different dynamic modes: mode I—bouncing and then coalescence, mode II—stripping and viscous separation of the coated nanoparticles, and mode III—tunneling and totally passing through the film.

3.2.1. Bouncing Dynamics. The kinetic energy is relatively low (v_0 < 0.62 m/s for d = 2.9 mm) in a bouncing event (Movies S1 and S2). The LM oscillates over the film until it coalesces with the film. This observation is consistent with the fluid trampoline.[33] The kinetic energy is primarily converted into the surface energy of the distorted film during impact. The bulk of this energy is then restored into the kinetic energy of the LM. Although some particles do indeed shed upon the first bounce, LM bounces upward rather than coalescing with the liquid film due to the hydrophobicity of particles and the existence of an air layer (Figure 4a). Different from the pure droplets, the air layer refers to the air retained in the particle gaps. With the successive bouncing, the coated particles are modified by the surfactant, leading to the cracking of the air layer and coalescence of the LM with the film. Such transition from the bouncing decay to coalescence is controlled by the resistance from the air layer[34] and modification rate of the particles. The air layer provides the air cushion with transient stability against extrusion, mediates momentum transfer, and consumes a considerable part of energy.[35] After impacting, the LM becomes oblate but recovers a nearly spherical shape when the soap film reaches the maximum elongation deformation. The bouncing strength decreases gradually and finally coalesces with the film at 259 ms, and the nanoparticles desorb from the LM surface (Figure 4b,c). Compared to the drop impact on the liquid film,[33] the partial coalescence is not observed and the coalescence duration is extended due to the good stability of the LM. The falling height that can meet the bouncing modes decreases with the increase of the LM diameter (Figure 4d). The gravity of the LM increases with the diameter, so it is necessary to reduce the inertial force by decreasing the height to achieve force balance. The dynamic trajectories of the LMs with diameters of 2.3 and 2.9 mm show irregular oscillation with small peaks between 100 and 150 ms, which is due to the oscillation frequency of the film being greater than the bouncing frequency. With the increase of the diameter and decrease of the height, both frequencies tend to be the same, so the trajectory exhibits a smooth curve.

https://doi.org/10.1021/acs.langmuir.1c02994
Langmuir 2022, 38, 2055−2065

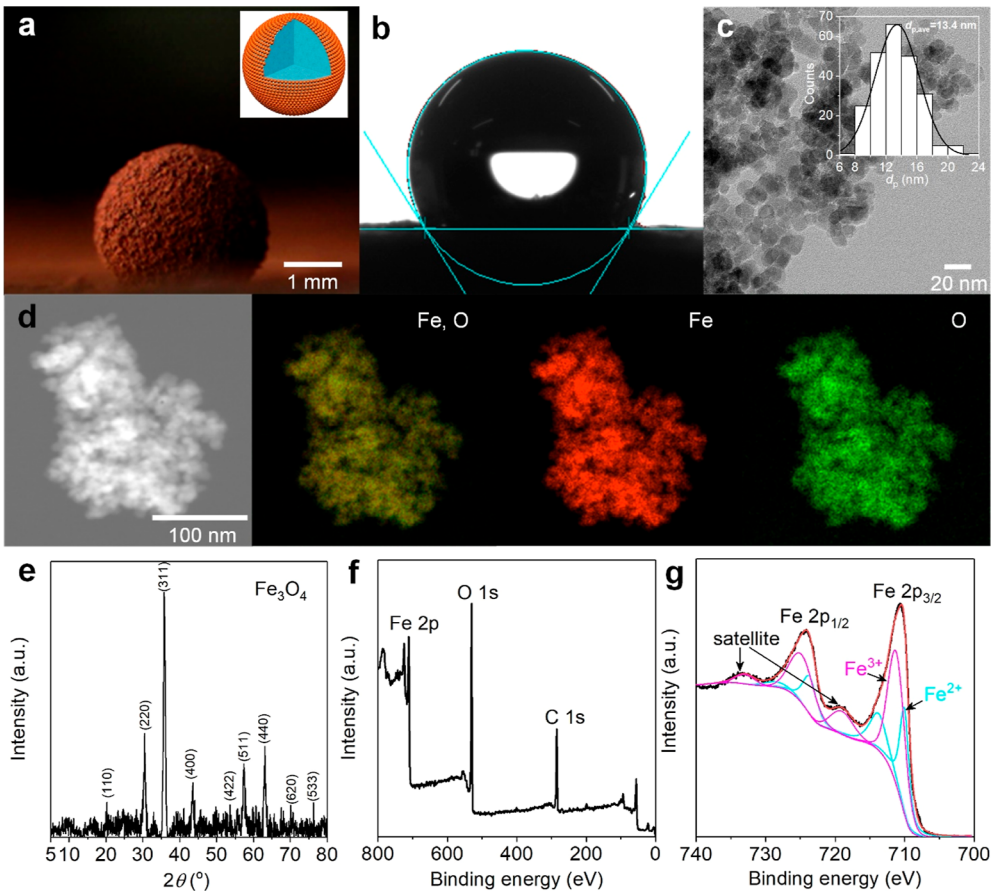

Figure 2. (a) Liquid marble sitting on a glass substrate. (b) Contact angle of hydrophobic Fe_3O_4 particles. (c) TEM image and size distribution of the particles. (d) EDS mapping images of the sample. (e) XRD and (f) XPS patterns of the particle aggregates. (g) XPS spectrum of Fe.

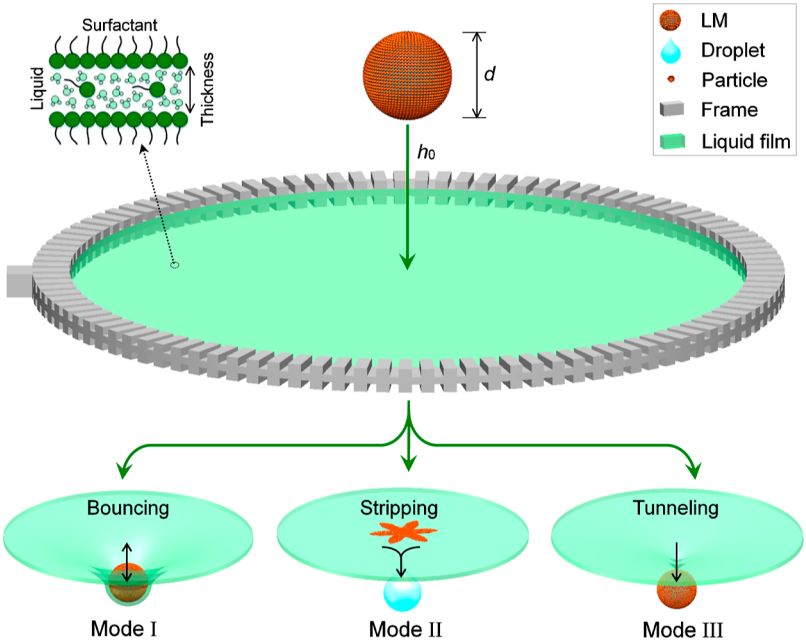

Figure 3. Concept of viscous separation showing different modes of the LM impact on the soap film: mode I-bouncing, mode II-stripping, and mode III-tunneling.

3.2.2. Stripping Dynamics. Increasing the impact velocity ($0.62 < v_0 < 0.77$ m/s for $d = 2.9$ mm) leads to the particles peeling off from the LM in a stripping event (Movies S3 and S4). The resistance pressure causes the LM to compress and deform, and the particles beneath are subject to the viscous drag force from the film. When the drag force is greater than

https://doi.org/10.1021/acs.langmuir.1c02994
Langmuir 2022, 38, 2055−2065

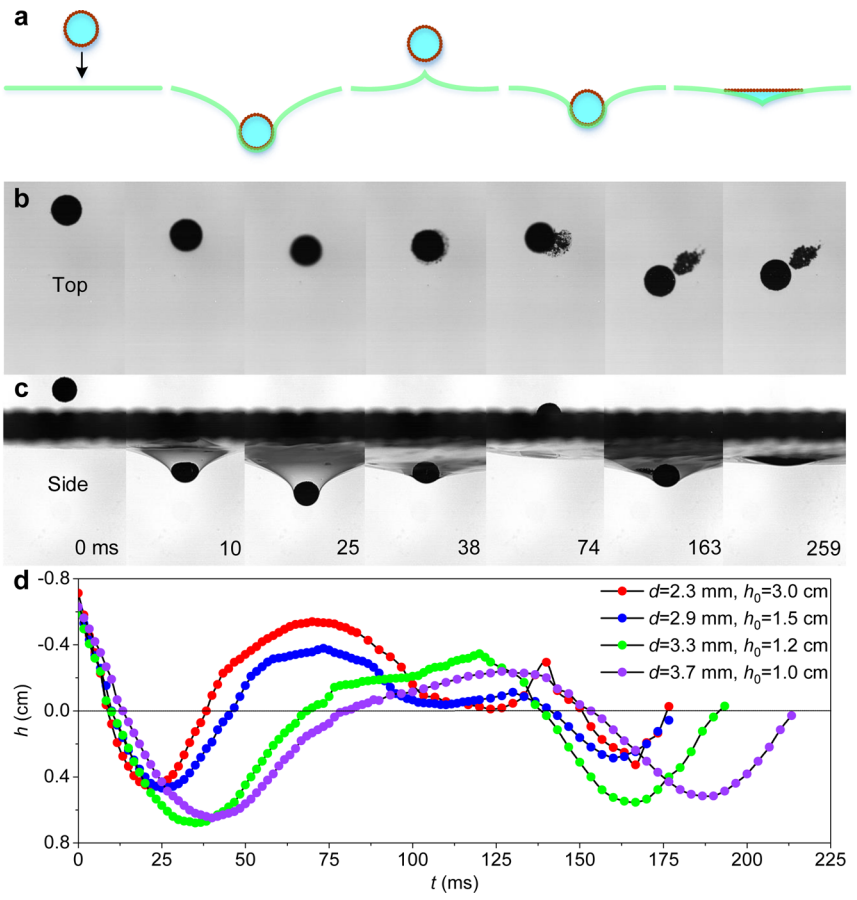

Figure 4. Bouncing dynamics of mode I. (a) Schematic diagram. (b) Top-view and (c) side-view sequential images for the case of d = 2.9 mm and h_0 = 1.5 cm. (d) Dynamic trajectory of the LM at various d and h_0 (h is the distance from the centroid of the LM to the equilibrium position of the liquid film).

the attractive force between particles, the particle crust is ruptured (Figure 5a), and thus, the water drop flows out via the opening gap. The liquid film continues to stretch downward under the action of gravity and inertial force until it reaches the elongation limit at t = 21 ms, then gradually relaxes back to its initial state, and self-heals the opening hole on the film. Subsequently, as the LM continues to fall, the particle crust detaches from the LM surface and gradually transfers onto the soap film under the viscoelastic action (Figure 5b,c).[36] After the detachment, the particle transport can be distinguished into two stages: first, contraction and then diffusion (Figure 5b). This is due to the variation of force directions under the stretching and bouncing actions of the film. The separation points delay and the oscillation amplitudes increase with the increase of the LM diameter due to the decrease of the falling height (Figure 5d). Due to the viscous resistance, the falling velocity sharply decreases when it makes contact with the film, especially during the separation stage. No remarkable differences can be detected in the transmittance spectra of separated water and deionized water, which confirms that no particles present in the separated water and the coated particles can be fully peeled off from the LM (Figure 6). Although the continuous operation of particle separation has been achieved in a successive stripping process (Figure 7 and Movie S7), the process is very complex and difficult to control due to complex periodic states and chaotic nature of the stripping behaviors.

3.2.3. Tunneling Dynamics. The kinetic energy determines whether the LM can pass through the film or not, and thus, a critical velocity exists for each case. In a tunneling event (Movies S5 and S6), the soap film is not able to absorb the initial kinetic energy of the LM. The film deforms into a pocket due to gravity and the inertial force of the LM (Figure 8a). This pocket then pinches off at the top of the LM and forms a liquid shell packing the LM.[37] The film reforms as the LM passes through, and the analogous self-healing effect can be observed in Figure 8b.[38] The energy barrier of the liquid film and the elastic potential energy of the LM cause the LM to deform back and forth (Figure 8c). According to the energy minimization principle,[39] when the contact line crosses the equator upward, the liquid film shrinks above the LM to form a hyperbolic neck (Figure 8c). As the LM descends, the neck shrinks rapidly and closes, forming a liquid filament (Figures 8b,c). At this moment, the film barrier disappears since the pulling force approaches zero, and the LM begins to fall freely again. Unlike the drop oscillation passing through the liquid film, the LM always maintains spherical falling with a liquid shell due to its rough surfaces and strong surface potential energy.[40,41] By calculating the derivation of the falling height ($v = \frac{dh}{dt}$), it can be known that the falling velocity first decreases and then increases, and the smaller the diameter is, the more obvious the change is (Figure 8d). The velocity decrease at the initial stage of impact is due to the viscous dissipation from dynamic wetting.[42] Large-size LMs can pass through the liquid

https://doi.org/10.1021/acs.langmuir.1c02994
Langmuir 2022, 38, 2055−2065

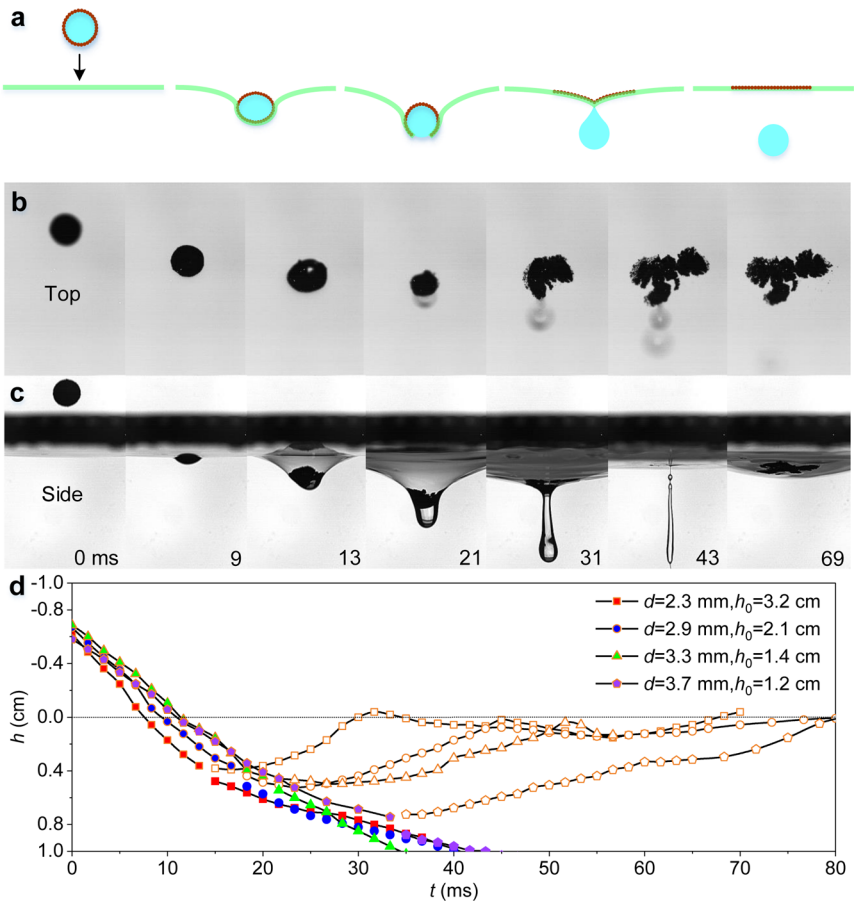

Figure 5. Stripping dynamics of mode II. (a) Schematic diagram. (b) Top-view and (c) side-view sequential images for the case of d = 2.9 mm and h_0 = 2.0 cm. (d) Dynamic trajectory of the LM at various d and h_0 (the uncolored open symbols represent the trajectory of the particle layer after stripping).

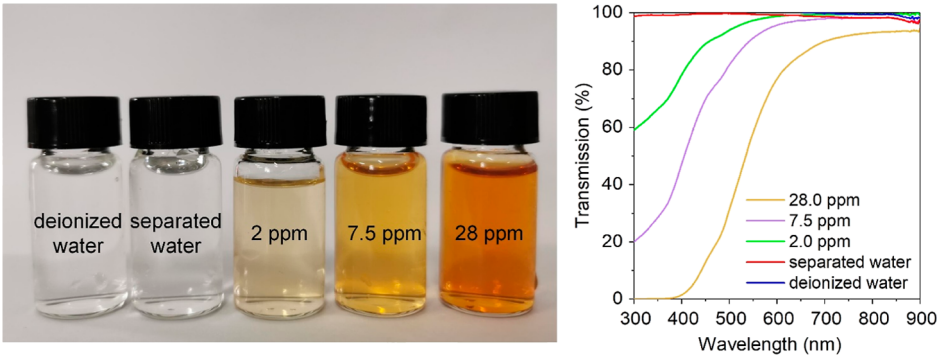

Figure 6. Transmission spectrum of the nanofluids with different concentrations (~2, 7.5, and 28 ppm) and the separated water from the LM and deionized water.

film at a low initial height since gravity provides more driving force.

3.3. Some Analysis of the Impact Process. In this section, we conduct energy, nondimensional, and mechanical analysis of the impact process to gain insights and physical mechanisms for particle separation.

3.3.1. Energy Analysis. To determine the mechanisms that dictate whether the coated particles can be peeled off or pass through the film, we systematically added LMs with different diameters dropwise into the liquid film from different heights and traced the corresponding dynamic processes (Table 2). To gain physical insights into the separation mechanism and criteria, we compared the magnitudes of the kinetic energy (E_k) of the LMs at impact to the other forms of energy, such as the maximum increase in the film surface energy due to stretching (E_s)[43] and energy dissipation (E_d) due to the viscous effects and LM deformation. In our experiments, the capillary number Ca was ~10^{-1}, indicating that the viscous effects were significant compared to the surface tension effects and therefore cannot be neglected.

As the LM impacts the film, it stretches the film, converting the kinetic energy into film surface energy. The viscous effect between the LM and film leads to the energy dissipation. When the LM drops from a certain height falling onto the

https://doi.org/10.1021/acs.langmuir.1c02994
Langmuir 2022, 38, 2055−2065

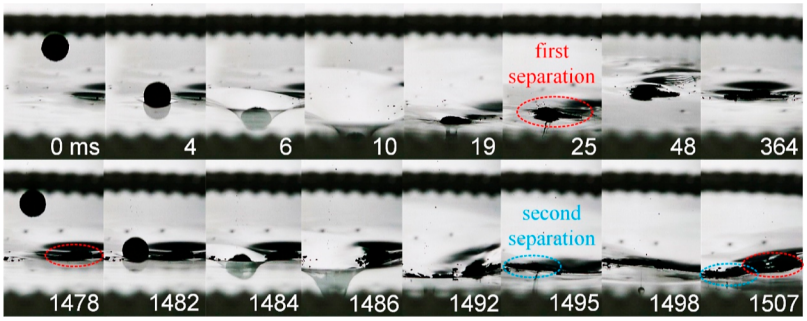

Figure 7. Successive stripping process for continuous particle separation.

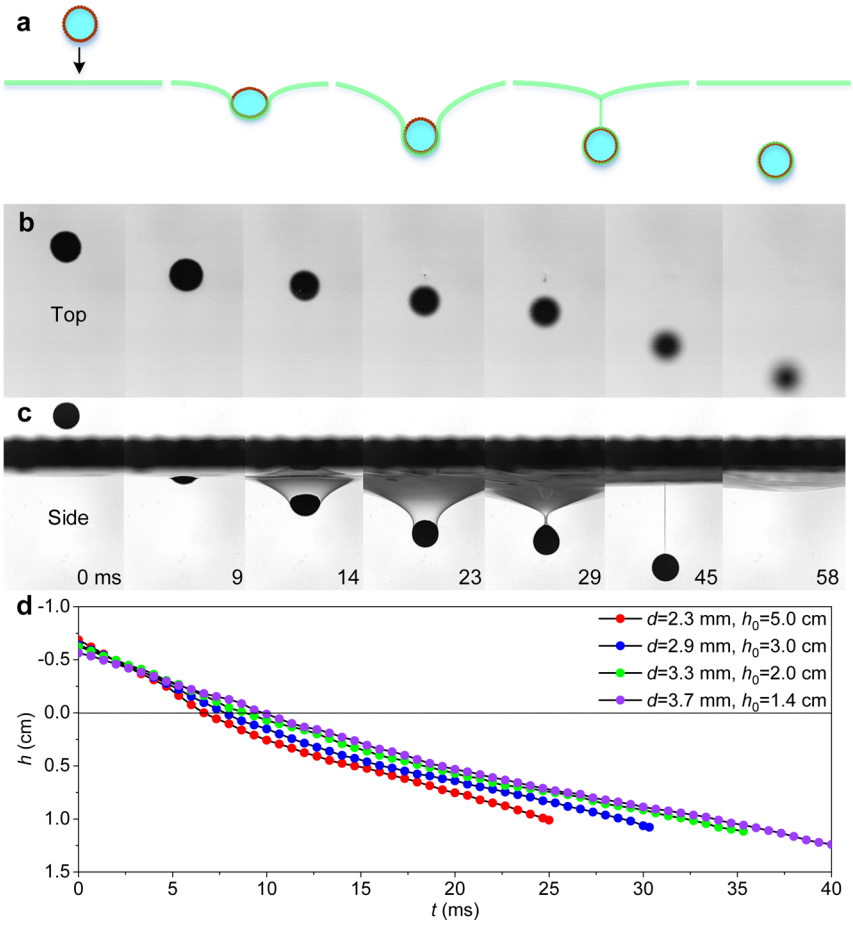

Figure 8. Tunneling dynamics of mode III. (a) Schematic diagram. (b) Top-view and (c) side-view sequential images for the case of d = 2.9 mm and h_0 = 2.2 cm. (d) Dynamic trajectory of the LM at various d and h_0.

liquid film, the initial kinetic energy (E_k) of the LM is expressed as

$$E_k = \frac{1}{2}mv_0^2 = mgh_0 = \frac{1}{6}\pi\rho g h_0 d^3 \quad (1)$$

where m is the mass of the LM, v_0 is the impacting velocity, h_0 is the initial falling height, and d is the LM diameter. Besides, the film approaches to forming a catenoid shape when slow-moving LMs impact the liquid films. The maximum change in surface energy (E_s) due to the film stretching is approximated to be the difference between the maximum area the film can stretch and the area of flat film of the outer radius R_f. This change in surface energy is approximated as

$$E_s = C\pi\sigma R_b^2(\sin h\,\varphi + \varphi) - 2\pi\sigma R_f^2 \quad (2)$$

where $\varphi = 2\cdot\text{acosh}\left(\frac{R_f}{R_b}\right)$, R_b is the radius of the LM, R_f is the radius of the liquid film, and C is a correction factor ~1.0027 to make the maximum film stretch area close to the experimental data.

The energy lost due to viscous dissipation reaches a maximum value as the LM approaches its maximum deformation. According to the Pasandideh-Fard model, the viscous dissipation energy (E_d) can be expressed as[44,45]

$$E_d = \frac{\pi}{3}\rho_m v_0^2 d d_{max}^2 \frac{1}{\sqrt{Re}} \quad (3)$$

https://doi.org/10.1021/acs.langmuir.1c02994
Langmuir 2022, 38, 2055−2065

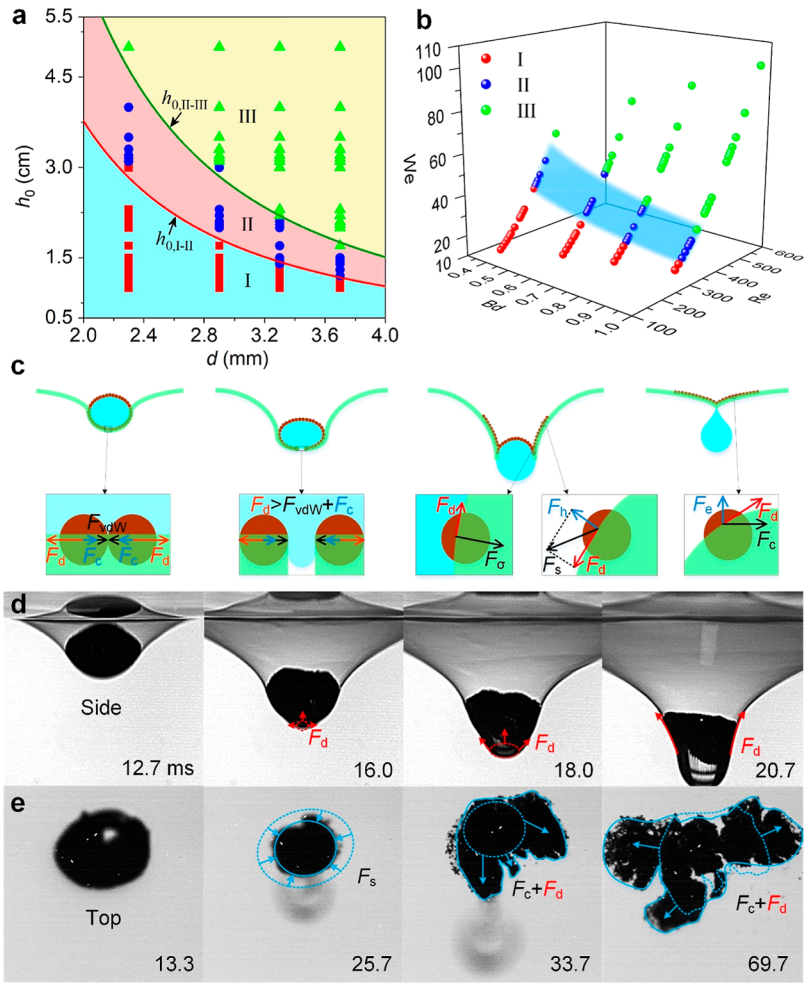

Figure 9. (a) Regime map derived from the experimental results and the separation thresholds for successful stripping. (b) Regime map based on nondimensional analysis. (c) Mechanical analysis for understanding the particle separation and diffusion. (d) Particle stripping (e) and transport process.

where ρ_m is the density of the LM, d_{max} is the maximum diameter of the expanded LM, and Re is the Reynolds number of the LM. To simplify the calculation, d_{max} and $1/\sqrt{Re}$ can be regarded as linear equations varying with d, based on the experimental data, which are $d_{max} = 1.44d$ and $1/\sqrt{Re} = -8.64d + 0.105$, respectively.

The three modes can be distinguished by the competitive relationships among E_k, E_s, and E_d. When the kinetic energy of the LM is less than the maximum change of the surface energy of the liquid film ($E_k < E_s$), the LM bounces on the liquid film, leading to mode I. When the kinetic energy of the LM is greater than the sum of the maximum variation of the surface energy in the liquid film and the viscous dissipation energy ($E_k > E_s + E_d$), the LM will break through the barrier of the film and continue to fall freely, which is mode III. When $E_s < E_k < E_s + E_d$, the particle layer ruptures and transfers to the liquid film under the action of viscous force, while the inside liquid passes through the film, leading to the stripping dynamics of mode II. By the energy balance, we obtained the thresholds as in Figure 9a

$$h_{0,I-II} = \frac{3\sigma[Cd^2(\sinh\phi + \phi) - 8R_f^2]}{2\rho g d^3} \quad (4)$$

$$h_{0,II-III} \approx \frac{3\sigma[Cd^2(\sinh\phi + \phi) - 8R_f^2]}{\rho g d^3(1.04 + 78.8d)} \quad (5)$$

3.3.2. Nondimensional Analysis. From a kinetic point of view, the impact process is affected by gravity, surface tension, inertial force, and viscous force, and the separation process is controlled by a number of parameters such as the liquid density (ρ), viscosity (μ), surface tension (σ), LM diameter (d), gravitational acceleration (g), and impacting velocity (v_0). Generally, the physical description of the impact process is as follows

$$F(\sigma, \mu, v_0, d, \rho, g) = 0 \quad (6)$$

Based on the Π theorem,[46] choosing ρ, v_0, and d as basic quantities, nondimensional quantities can be formed

$$\pi_1 = \frac{\rho^{a_1} v_0^{b_1} d^{c_1}}{\sigma}, \qquad \pi_2 = \frac{\rho^{a_2} v_0^{b_2} d^{c_2}}{\mu}, \qquad \pi_3 = \frac{\rho^{a_3} v_0^{b_3} d^{c_3}}{g} \quad (7)$$

By substituting the basic dimensions into the physical quantities in π_1, we get the following results

https://doi.org/10.1021/acs.langmuir.1c02994
Langmuir 2022, 38, 2055−2065

$$MT^{-2} = (ML^{-3})^{a_1}(LT^{-1})^{b_1}L^{c_1} \quad (8)$$

According to the principle of dimensional consistence, the exponent is obtained: $a_1 = 1$, $b_1 = 2$, and $c_1 = 1$. Therefore, π_1 is expressed as

$$\pi_1 = \frac{\rho v_0^2 d}{\sigma} = We \quad (9)$$

where $We = \rho v_0^2 d/\sigma$ is the Weber number (ratio of the inertial force to the surface tension). Similarly, π_2 and π_3 are expressed as

$$\pi_2 = \frac{\rho v d}{\mu} = Re \quad (10)$$

$$\pi_3 = \frac{v^2}{gd} = Fr = \frac{We}{Bd} \quad (11)$$

where $Re = \rho v_0 d/\mu$ is the Reynolds number (ratio of the inertial force to the viscous force) and $Bd = \rho g d^2/\sigma$ is the Bond number (ratio of gravity to the surface tension). Thus, the nondimensional relationship is expressed as

$$f(\pi_1, \pi_2, \pi_3) = f(We, Re, Bd) = 0 \quad (12)$$

Three nondimensional numbers are derived via nondimensional analysis: *We*, *Re*, and *Bd*. A regime map built on nondimensional numbers offers more general information for the separation criteria, and the separation region is marked as $We = 0.00028 \cdot Bd^{-0.488} Re^{2.020}$ (blue region in Figure 9b).

3.3.3. Mechanical Analysis. We can get more insights into particle separation and transport by mechanical analysis. The cracking of the particle crust initiates during the ongoing deformation of the LM. The internal liquid then drips out, and the particles that are viscoelastic are transported to the film. We ascribe this breakup of the particle aggregates to the viscous hydrodynamics of the particle-armed fluid interface, which represents the mechanical property of the interface responding to external deformations with a shear mode.[47] The resulting viscous drag force on a particle can be expressed as

$$F_d = 6\pi\mu v_0 r_p \quad (13)$$

where μ is the viscosity of the film and r_p is the particle radius, ~6.7 nm. The interaction between particles includes electrostatic repulsions, London−van der Waals forces, capillary interactions, and steric interactions, depending on the properties of the fluids and of the particles.[48] However, SDS greatly reduces the electrostatic repulsion between the particles,[49] and the steric interaction only accounts for colloidal particles with the polymer interface.[50] Thus, two attractive forces should be considered in our experiment: van der Waals and capillary forces. The van der Waals force is written as follows[51]

$$F_{vdW} = -\frac{A_{eff}}{12}\frac{r_p}{D^2} \quad (14)$$

where A_{eff} is the effective Hamaker constant ~1.37×10^{-20} J[52] and $D = z - 2r_p$ is the separation surface ~0.12 nm at contact. The capillary force is[53]

$$F_{cap} \approx -12\pi\sigma H_2^2 \cos[2(\phi_A + \phi_B)]\frac{4r_{pc}^4}{z^5} \quad (15)$$

where H_2 is the amplitude of the (quadrupolar) undulations of the contact line ~1 nm, $\phi_{A,B}$ is the orientation angle of the particles relative to the line centers, and the particle size is too small compared to the LM, so $\cos[2(\phi_A + \phi_B)] \approx 1$; $r_{pc} = r_p \cdot \sin\theta$ is the radius of the contact line, and z is the distance between the particle centers. Thus, when the impact velocity exceeds a critical value, $F_d > F_{vdW} + F_{cap}$, the drag force drives the cracking of particle aggregates, leading to the rupture of the particle crust (Figures 9c,d). By combining eqs 13−15, the critical velocity can be calculated as 0.64 m/s for d = 2.9 mm.

For the particle transport, the falling velocity of the LM is much faster than that of the film. Thus, the particles move upward relative to the LM under the actions of the viscous force (F_d) and surface tension (F_σ) so that the particles transfer to the surface of the liquid film. When the film approaches the deformation saturation, the trapped particles converge to the center under the action of the shrink force (F_s), which is the combination of the viscous force (F_d) and the holding force (F_h). F_h is the vertical force exerted by the liquid film on particles, which mainly comes from buoyancy and elasticity. When the film rebounds upward, the particles are affected by the upward elastic force (F_e), the viscous force (F_d) parallel to the film, and the outward capillary force (F_c), in which F_c is the resultant force of surface tension and capillary influence on particles. Thus, the particles diffuse and scatter outward along the film (Figure 9c,e).

4. CONCLUSIONS

In summary, we show that a free-standing soap film can be facilely engineered to completely separate the particles from the liquid surface, resulting in at least two unique contributions: first, we present visual evidence of dynamic modes of the bouncing, stripping, and tunneling process from LMs' impact on the soap film; second, the threshold of viscous separation with a splash is identified from the energy analysis. The results indicate a strong correlation between the particle separation, impact velocity, variation of surface energy, and viscous dissipation. The separation criteria based on *We*, *Re*, and *Bd* are identified via nondimensional analysis. The threshold model and separation criteria validated with comprehensive experiments provide a quantitative guide for the material choice and operating conditions for scalable particle recycling with high yield.

However, there are a few limitations of this work that are yet to be explored. First, the viscous effect between the LM and liquid film is the key mechanism for the separation of particles from the internal liquid. Further investigation of successive collision is necessary to understand the potential for the continuous operation of the process. Second, the capillary interaction or energy associated with particle adsorption varies with the particle size, morphology, and surface properties. Different materials with diverse sizes and morphologies should be extensively studied to better understand the interfacial stress and viscous behavior on particle separation. Furthermore, in this study, we focused on the novel mechanism of particle separation rather than in-depth exploring the particle transport. This discovery will lead to additional work investigating the transport and fate of these particles in the environment.

■ ASSOCIATED CONTENT

Supporting Information

The Supporting Information is available free of charge at https://pubs.acs.org/doi/10.1021/acs.langmuir.1c02994.

https://doi.org/10.1021/acs.langmuir.1c02994
Langmuir 2022, 38, 2055−2065

Description of Movies S1−7 (PDF)
Side view of mode I (MP4)
Top view of mode I (MP4)
Side view of mode II (MP4)
Top view of mode II (MP4)
Side view of mode III (MP4)
Top view of mode III (MP4)
Successive stripping process for continuous particle separation (MP4)

AUTHOR INFORMATION

Corresponding Authors

Guohua Liu − *Beijing Key Laboratory of Multiphase Flow and Heat Transfer for Low Grade Energy Utilization, North China Electric Power University, Beijing 102206, P.R. China;* orcid.org/0000-0003-3401-1851; Email: liuguohua126@126.com

Jinliang Xu − *Beijing Key Laboratory of Multiphase Flow and Heat Transfer for Low Grade Energy Utilization, North China Electric Power University, Beijing 102206, P.R. China;* orcid.org/0000-0003-0145-9983; Email: xjl@ncepu.edu.cn

Authors

Yijun Feng − *Beijing Key Laboratory of Multiphase Flow and Heat Transfer for Low Grade Energy Utilization, North China Electric Power University, Beijing 102206, P.R. China*

Kaiying Wang − *Department of Microsystems, University of South-Eastern Norway, Horten 3184, Norway;* orcid.org/0000-0002-0018-0959

Wenbin Mao − *Department of Mechanical Engineering, University of South Florida, Tampa, Florida 33620, United States*

Guansheng Yao − *Beijing Key Laboratory of Multiphase Flow and Heat Transfer for Low Grade Energy Utilization, North China Electric Power University, Beijing 102206, P.R. China*

Complete contact information is available at: https://pubs.acs.org/10.1021/acs.langmuir.1c02994

Notes

The authors declare no competing financial interest.

ACKNOWLEDGMENTS

This research was supported by the Natural Science Foundation of China (52076077 and 51821004).

REFERENCES

(1) Bernard, P. B.; Tommy, S. H. *Colloidal Particles at Liquid Interfaces*; Cambridge University: New York, USA, 2006.

(2) Landel, J. R.; Wilson, D. I. The Fluid Mechanics of Cleaning and Decontamination of Surfaces. *Annu. Rev. Fluid. Mech.* **2021**, *53*, 147−171.

(3) Song, G.; Kenney, M.; Chen, Y.-S.; Zheng, X.; Deng, Y.; Chen, Z.; Wang, S. X.; Gambhir, S. S.; Dai, H.; Rao, J. Carbon-coated FeCo nanoparticles as sensitive magnetic-particle-imaging tracers with photothermal and magnetothermal properties. *Nat. Biomed. Eng.* **2020**, *4*, 325−334.

(4) Mezzenga, R.; Schurtenberger, P.; Burbidge, A.; Michel, M. Understanding foods as soft materials. *Nat. Mater.* **2005**, *4*, 729−740.

(5) Binks, B. P.; Murakami, R. Phase inversion of particle-stabilized materials from foams to dry water. *Nat. Mater.* **2006**, *5*, 865−869.

(6) Erb, R. M.; Son, H. S.; Samanta, B.; Rotello, V. M.; Yellen, B. B. Magnetic assembly of colloidal superstructures with multipole symmetry. *Nature* **2009**, *457*, 999−1002.

(7) Zhao, Z.; Qin, S.; Wang, D.; Pu, Y.; Wang, J.-X.; Saczek, J.; Harvey, A.; Ling, C.; Wang, S.; Chen, J.-F. Multi-stimuli-responsive liquid marbles stabilized by superhydrophobic luminescent carbon dots for miniature reactors. *Chem. Eng. J.* **2020**, *391*, 123478.

(8) Ward, S. G. Froth Flotation of Minerals. *Nature* **1956**, *178*, 712−713.

(9) Dinsmore, A. D.; Hsu, M. F.; Nikolaides, M. G.; Marquez, M.; Bausch, A. R.; Weitz, D. A. Colloidosomes: selectively permeable capsules composed of colloidal particles. *Science* **2002**, *298*, 1006−1009.

(10) He, M.; Gales, J. P.; Ducrot, É.; Gong, Z.; Yi, G.-R.; Sacanna, S.; Pine, D. J. Colloidal diamond. *Nature* **2020**, *585*, 524−529.

(11) Liu, L.; Pan, Y.; Bhushan, B.; Li, F.; Zhao, X. Core-shell magnetic nanoparticles for substrate-Independent super-amphiphobic surfaces and mechanochemically robust liquid marbles. *Chem. Eng. J.* **2020**, *391*, 123523.

(12) Crossley, S.; Faria, J.; Shen, M.; Resasco, D. E. Solid Nanoparticles that Catalyze Biofuel Upgrade Reactions at the Water/Oil Interface. *Science* **2010**, *327*, 68−72.

(13) Luo, D.; Wang, F.; Zhu, J.; Cao, F.; Liu, Y.; Li, X.; Willson, R. C.; Yang, Z.; Chu, C.-W.; Ren, Z. Nanofluid of graphene-based amphiphilic Janus nanosheets for tertiary or enhanced oil recovery: High performance at low concentration. *Proc. Natl. Acad. Sci. U.S.A.* **2016**, *113*, 7711−7716.

(14) Terfort, A.; Bowden, N.; Whitesides, G. M. Three-dimensional self-assembly of millimetre-scale components. *Nature* **1997**, *386*, 162−164.

(15) Lin, Y.; Skaff, H.; Emrick, T.; Dinsmore, A. D.; Russell, T. P. Nanoparticle Assembly and Transport at Liquid-Liquid Interfaces. *Science* **2003**, *299*, 226−229.

(16) Ballard, N.; Law, A. D.; Bon, S. A. F. Colloidal particles at fluid interfaces: behaviour of isolated particles. *Soft Matter* **2019**, *15*, 1186−1199.

(17) Liu, Z.; Zhang, Y.; Chen, C.; Yang, T.; Wang, J.; Guo, L.; Liu, P.; Kong, T. Larger Stabilizing Particles Make Stronger Liquid Marble. *Small* **2019**, *15*, No. e1804549.

(18) Manikantan, H.; Squires, T. M. Surfactant dynamics: hidden variables controlling fluid flows. *J. Fluid Mech.* **2020**, *892*, P1.

(19) Forth, J.; Kim, P. Y.; Xie, G.; Liu, X.; Helms, B. A.; Russell, T. P. Building Reconfigurable Devices Using Complex Liquid-Fluid Interfaces. *Adv. Mater.* **2019**, *31*, No. e1806370.

(20) Megens, M.; Aizenberg, J. Like-charged particles at liquid interfaces. *Nature* **2003**, *424*, 1014.

(21) Nikolaides, M. G.; Bausch, A. R.; Hsu, M. F.; Dinsmore, A. D.; Brenner, M. P.; Gay, C.; Weitz, D. A. Electric-field-induced capillary attraction between like-charged particles at liquid interfaces. *Nature* **2002**, *420*, 299−301.

(22) Martínez-Pedrero, F. Static and dynamic behavior of magnetic particles at fluid interfaces. *Adv. Colloid Interface Sci.* **2020**, *284*, 102233.

(23) Tavacoli, J. W.; Katgert, G.; Kim, E. G.; Cates, M. E.; Clegg, P. S. Size limit for particle-stabilized emulsion droplets under gravity. *Phys. Rev. Lett.* **2012**, *108*, 268306.

(24) Abkarian, M.; Protière, S.; Aristoff, J. M.; Stone, H. A. Gravity-induced encapsulation of liquids by destabilization of granular rafts. *Nat. Commun.* **2013**, *4*, 1895.

(25) Poulichet, V.; Garbin, V. Cooling Particle-Coated Bubbles: Destabilization beyond Dissolution Arrest. *Langmuir* **2015**, *31*, 12035−12042.

(26) Poulichet, V.; Garbin, V. Ultrafast desorption of colloidal particles from fluid interfaces. *Proc. Natl. Acad. Sci. U.S.A.* **2015**, *112*, 5932−5937.

(27) Chen, Z.; Zang, D.; Zhao, L.; Qu, M.; Li, X.; Li, X.; Li, L.; Geng, X. Liquid Marble Coalescence and Triggered Microreaction Driven by Acoustic Levitation. *Langmuir* **2017**, *33*, 6232−6239.

(28) Zang, D.; Li, J.; Chen, Z.; Zhai, Z.; Geng, X.; Binks, B. P. Switchable Opening and Closing of a Liquid Marble via Ultrasonic Levitation. *Langmuir* **2015**, *31*, 11502−11507.

(29) Aussillous, P.; Quéré, D. Liquid marbles. *Nature* **2001**, *411*, 924−927.
(30) Zhao, Y.; Fang, J.; Wang, H.; Wang, X.; Lin, T. Magnetic liquid marbles: manipulation of liquid droplets using highly hydrophobic Fe_3O_4 nanoparticles. *Adv. Mater.* **2010**, *22*, 707−710.
(31) Meier, M.; Hulva, J.; Jakub, Z.; Pavelec, J.; Setvin, M.; Bliem, R.; Schmid, M.; Diebold, U.; Franchini, C.; Parkinson, G. S. Water agglomerates on Fe_3O_4(001). *Proc. Natl. Acad. Sci. U.S.A.* **2018**, *115*, No. E5642.
(32) Patsyk, A.; Sivan, U.; Segev, M.; Bandres, M. A. Observation of branched flow of light. *Nature* **2020**, *583*, 60−65.
(33) Gilet, T.; Bush, J. W. M. The fluid trampoline: droplets bouncing on a soap film. *J. Fluid Mech.* **2009**, *625*, 167−203.
(34) Tang, X.; Saha, A.; Law, C. K.; Sun, C. Bouncing drop on liquid film: Dynamics of interfacial gas layer. *Phys. Fluids* **2019**, *31*, 013304.
(35) de Ruiter, J.; Lagraauw, R.; van den Ende, D.; Mugele, F. Wettability-independent bouncing on flat surfaces mediated by thin air films. *Nat. Phys.* **2014**, *11*, 48−53.
(36) Zhang, Y.; Yin, M.; Baek, Y.; Lee, K.; Zangari, G.; Cai, L.; Xu, B. Capillary transfer of soft films. *Proc. Natl. Acad. Sci. U.S.A.* **2020**, *117*, 5210−5216.
(37) Kumar, D.; Paulsen, J. D.; Russell, T. P.; Menon, N. Wrapping with a splash: High-speed encapsulation with ultrathin sheets. *Science* **2018**, *359*, 775−778.
(38) Taylor, G. I.; Michael, D. H. On making holes in a sheet of fluid. *J. Fluid Mech.* **1973**, *58*, 625−639.
(39) Pysh, E. S. Conformations at Local Energy Minimums for Gramicidin S: Optical Calculations. *Science* **1970**, *167*, 290−292.
(40) Timounay, Y.; Pitois, O.; Rouyer, F. Gas Marbles: Much Stronger than Liquid Marbles. *Phys. Rev. Lett.* **2017**, *118*, 228001.
(41) Zou, J.; Wang, W.; Ji, C.; Pan, M. Droplets passing through a soap film. *Phys. Fluids* **2017**, *29*, 062110.
(42) Andreotti, B.; Snoeijer, J. H. Statics and Dynamics of Soft Wetting. *Annu. Rev. Fluid. Mech.* **2020**, *52*, 285−308.
(43) Stogin, B. B.; Gockowski, L.; Feldstein, H.; Claure, H.; Wang, J.; Wong, T. S. Free-standing liquid membranes as unusual particle separators. *Sci. Adv.* **2018**, *4*, No. eaat3276.
(44) Pasandideh-Fard, M.; Qiao, Y. M.; Chandra, S.; Mostaghimi, J. Capillary effects during droplet impact on a solid surface. *Phys. Fluids* **1996**, *8*, 650−659.
(45) Vadillo, D. C.; Soucemarianadin, A.; Delattre, C.; Roux, D. C. D. Dynamic contact angle effects onto the maximum drop impact spreading on solid surfaces. *Phys. Fluids* **2009**, *21*, 122002.
(46) Buckingham, E. On Physically Similar Systems; Illustrations of the Use of Dimensional Equations. *Phys. Rev.* **1914**, *4*, 345−376.
(47) Ji, X.; Wang, X.; Zhang, Y.; Zang, D. Interfacial viscoelasticity and jamming of colloidal particles at fluid-fluid interfaces: a review. *Rep. Prog. Phys.* **2020**, *83*, 126601.
(48) Poulichet, V. P. *Colloid-Stabilised Bubbles: Particle Expulsion Triggered by External Fields*; Imperial College London: London, 2016.
(49) Park, B. J.; Pantina, J. P.; Furst, E. M.; Oettel, M.; Reynaert, S.; Vermant, J. Direct Measurements of the Effects of Salt and Surfactant on Interaction Forces between Colloidal Particles at Water−Oil Interfaces. *Langmuir* **2008**, *24*, 1686−1694.
(50) Dickinson, E.; Eriksson, L. Particle flocculation by adsorbing polymers. *Adv. Colloid Interface Sci.* **1991**, *34*, 1−29.
(51) Israelachvili, J. N. *Intermolecular and Surface Forces*; Elsevier, 2011.
(52) Prieve, D. C.; Russel, W. B. Simplified predictions of Hamaker constants from Lifshitz theory. *J. Colloid Interface Sci.* **1988**, *125*, 1−13.
(53) Stamou, D.; Duschl, C. Long-range attraction between colloidal spheres at the air-water interface-the consequence of an irregular meniscus. *Phys. Rev. E: Stat. Phys., Plasmas, Fluids, Relat. Interdiscip. Top.* **2000**, *64*, 5263−6271.

https://doi.org/10.1021/acs.langmuir.1c02994
Langmuir 2022, 38, 2055−2065